Velocity and pressure fields of SWBLIs on porous plates

Bas van Oudheusden[1]*, Arti Flinkerbusch[1], Ferry Schrijer[1]

[1]Delft University of Technology, Faculty of Aerospace Engineering, Delft, The Netherlands

* b.w.vanoudheusden@tudelft.nl

Abstract

The paper investigates the application of wall porosity for controlling the interaction between an impinging oblique shock wave and a turbulent boundary layer. This type of passive control aims to smear out the shock system in the longitudinal extent, thus inducing a more gradual pressure rise over the shock system with associated decrease of shock losses. Flow velocity measurements with PIV have been enhanced with pressure field information, obtained from integration of the governing equations. It is observed that the porosity indeed results in an extension of the upstream influence and, hence, increases the interaction length. Furthermore, the separation tendency in the interaction is increased, while the pressure rise inside the flow field is reduced. These effects increase in strength with porosity level, as expected, but are found to decrease with increasing hole diameter.

1 Introduction

The interaction of an impinging shock wave and a turbulent boundary layer (SWBLI) has particular significance in the high-speed flight regime (Dolling 2001, Babinsky & Harvey 2011). Means to mitigate the potentially adverse effects of these interactions have been explored by a variety of control techniques (Délery 1985, Délery and Bur 2000), including boundary layer bleed or suction, enhanced upstream mixing induced by various types of vortex generators (Panaras and Lu 2015, Titchener and Babinsky 2015) or by air jets (Souverein and Debiève 2010), plasma actuators (Webb et al. 2013), geometry modifications (Bruce and Colliss 2015, Gramola et al. 2018) or the application of surface porosity (Ragunathan 1988, Stanewsky et al. 1997). The working principle of the latter approaches is to smear out the interaction in the longitudinal extent, thus inducing a more gradual pressure rise over the shock system with associated decrease in shock losses. Implementation of passive control by means of a ventilated cavity, that provides a pressure communication over the interaction, has been reported using porous surfaces (McCormick 1993, Bur et al. 1998), as well as flexible surface flaps (Gefroh et al. 2002). This type of passive SWBLI control has mainly been reported for near-normal shock wave interactions, such as occurring for transonic airfoils or diffusors (Délery 1985, Ragunathan 1988), while its application is relative scarce for the impinging SWBLI geometry that is typical for supersonic intake configurations (Gefroh et al. 2002). Yet, also for these configurations the potential for reducing shock losses could be worthwhile to investigate.

The present paper reports on an experimental investigation of the effect of surface porosity on the interaction between an impinging oblique shock wave and a turbulent boundary layer. The basic configuration comprises a cavity covered by a perforated plate, where the level of porosity and hole diameter has been varied to assess the impact of these parameters. Particle Image Velocimetry (PIV) has been used as main diagnostic tool for flow velocity measurements, which have been further processed to obtain pressure field information, from integration of the governing equations (van Oudheusden 2008).

2   Experimental configuration

2.1 Flow facility and flow conditions

The experiments were carried out in the TUD ST-15 supersonic wind tunnel in a nominal Mach 2 configuration, with test section dimensions 152 mm (height) by 150 mm (width). For the current shock control investigation, an insert fixture was mounted to the wind tunnel bottom liner that could accommodate separate plates, in order to study the effect of ventilated cavities with different degrees of porosity (see Figure 1). Due to the presence of this insert the effective free-stream Mach number over the plate was reduced to 1.86. The tunnel was operated at a unit Reynolds number of 45 million, while the (undisturbed) boundary layer thickness ($\delta_{99,0}$) was measured to be 5.1 mm. The ventilated cavity underneath the porous surface has a depth of 7 mm (1.4 $\delta_{99,0}$) and extends over a length of 79 mm (15.6 $\delta_{99,0}$). The shock generator has a wedge angle of 8.8°, with the extrapolated shock impingement location at 63% of the cavity length. This position is taken as the origin of a Cartesian coordinate frame, with x the longitudinal and y the wall-normal coordinate. The undisturbed boundary layer thickness $\delta_{99,0}$ is used as scaling length. A summary of the freestream flow conditions and the characteristics of the undisturbed boundary layer can be found in Table 1 (integral properties are evaluated according to their incompressible flow definitions).
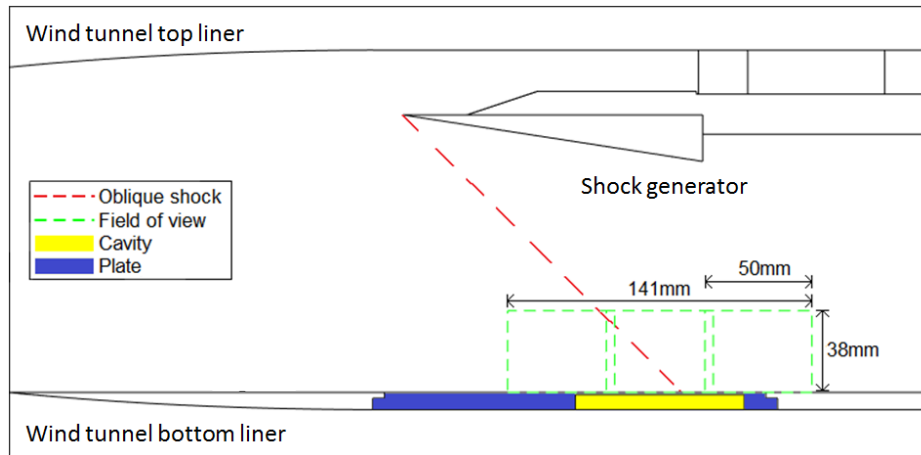

Figure 1: Wind tunnel arrangement with shock generator and ventilated cavity position and the field of view arrangement for the PIV measurements.

Table 1. Flow conditions and undisturbed boundary layer properties.

variable	value	variable	value
free stream Mach number M_∞	1.86	boundary layer thickness $\delta_{99,0}$	5.06±0.05 mm
free stream velocity U_∞	482 m/s	displacement thickness δ_i^*	0.51±0.03 mm
stagnation pressure p_0	320 kPa	momentum thickness θ_i	0.42±0.01 mm
stagnation temperature T_0	283 K	shape factor H_i	1.21±0.05
unit Re number	45×10^6 m^{-1}	$Re_{\theta i}$	19,000±500

2.2 Porous plate design

Four different porous plates (of thickness 1 mm) were investigated, with an additional solid "dummy" plate included as reference case representing the baseline uncontrolled SWBLI. The porosity of the plates was realized by means of circular holes that are arranged in a hexagonal pattern. Hole diameters of 0.5, 1.0 and 1.5 mm were used (i.e., 0.1 $\delta_{99,0}$ to 0.3 $\delta_{99,0}$) and porosity levels of 5% and 2.5% surface area. The characterization of the different porous plate properties is

given in Table 2, in terms of porosity (ε), hole diameter (d_h) and hole separation distance (s_h). Note that plates 1 to 3 have the same porosity, plates 2 and 4 have the same hole diameter (but different porosity), while plates 3 and 4 have nearly the same hole separation (but different hole diameter, hence, porosity). Using the method of Doerffer and Bohning (2000), the surface-averaged transpiration velocity is estimated to be about 2% of the freestream velocity for the 5% porosity cases.

Table 2: Porous plate characteristics

plate	porosity ε	hole diameter d_h	$\dfrac{d_h}{\delta_{99,0}}$	hole spacing s_h	$\dfrac{s_h}{\delta_{99,0}}$
#1	5%	0.5 mm	0.1	2.1 mm	0.4
#2	5%	1.0 mm	0.2	4.3 mm	0.8
#3	5%	1.5 mm	0.3	6.4 mm	1.3
#4	2.5%	1.0 mm	0.2	6.0 mm	1.2

2.3 Particle Image Velocimetry

Planar (2C) PIV measurements were performed in the centerline plane of the interaction. Illumination was provided by a Quantel Evergreen Nd:YAG laser (200 mJ/pulse) and DEHS was used as flow seeding. Imaging was performed with three Imperx Bobcat cameras (1624 × 1236 pixels) with a combined FOV of 141 mm × 38 mm (27.8 $\delta_{99,0}$ × 7.5 $\delta_{99,0}$), see Figure 1, at a digital resolution of 32.5 pix/mm. Image analysis was carried out with LaVision DaVis 8.4.0, using iterative multigrid cross correlation with a final window size of 24 × 24 pixels and 75% overlap, yielding a vector spacing of 0.18 mm (0.036 $\delta_{99,0}$) and a full FOV containing approximately 770 × 210 vectors.

For each configuration sequences of 300 double-frame image pairs were acquired at a recording rate of about 8 Hz, with a pulse separation of 1 μs. This corresponds to a free stream particle displacement of 0.5 mm, which is equivalent to 16 pixels. Assuming a cross-correlation uncertainty of 0.2 pixel, the corresponding uncertainty on the instantaneous velocity value is estimated as 6 m/s (which is about 1% of U_∞). In view of the ensemble size (N = 300), the statistical convergence uncertainty on the mean velocity is calculated to vary from 0.3 to 3 m/s (0.06% to 0.6% of U_∞) for velocity fluctuation levels ranging from 1% to 10% of U_∞, while the relative uncertainty on the r.m.s. of the velocity fluctuations is 5%.

2.4 Pressure computation

Pressure fields were derived from the velocity data by spatial integration of the pressure gradient (van Oudheusden 2013). This non-intrusive procedure provides access to surface and field pressure information, which in the present case is otherwise especially cumbersome to obtain in view of the wall porosity. The study of van Gent et al. (2018) has shown how time-average pressure can be obtained from velocity statistics by a Reynolds-averaging of the momentum equation, and that at moderate compressibility conditions density fluctuations and temperature spatial gradients can be neglected. It was furthermore verified that the contribution of the velocity fluctuations (Reynolds stresses) is small in the present case; a similar observation was made in the SWBLI case reported in van Oudheusden (2008). The flow can therefore be treated in the pressure computation as steady, such that the pressure represents the time-average pressure (similar for the other flow properties). Moreover, the flow is assumed to be approximately two-dimensional in view of the experimental geometry. The procedure of the pressure determination is shortly outlined below, while more details can be found in e.g. van Oudheusden (2008, 2013). The pressure gradient ∇p is related to the velocity field $\boldsymbol{u}$ through the momentum equation, while neglecting the viscous term:

$$\nabla p = -\rho(\boldsymbol{u}.\nabla)\boldsymbol{u}$$

The density is substituted from the gas law $\rho = p/RT$, yielding an explicit expression for the pressure gradient:

$$\frac{\nabla p}{p} = \nabla\ln(p/p_\infty) = -\frac{1}{RT}(\boldsymbol{u}.\nabla)\boldsymbol{u}$$

The temperature is inferred directly from the velocity field by assuming constant total temperature:

$$\frac{T}{T_\infty} = 1 + \frac{\gamma - 1}{2}M_\infty^2\left(1 - \frac{V^2}{V_\infty^2}\right)$$

Here γ is the specific heat ratio and $V = \|\boldsymbol{u}\|$ represents the velocity magnitude. Finally, the pressure is obtained by spatial integration of the pressure gradient, according to the procedure described in van Oudheusden (2008), starting from a region upstream of the interaction and outside of the boundary layer, where the pressure is prescribed assuming isentropic flow. The uncertainty on the resulting pressure values is estimated at approximately 2% of p_∞.

3   Results

3.1 Flow fields

Schlieren visualizations of the interaction are presented in Figure 2, for the reference interaction on the solid plate, as well as for two of the porous plates. The latter two represent the cases of the smallest and largest hole diameter considered in this investigation, which are 0.5 mm and 1.5 mm, and both with the same overall porosity level of 5%. The baseline interaction - diagram (a) – displays a thickening of the boundary layer over the interaction due to the pressure rise imposed by the impinging shock, with the origin of the reflected shock that marks the upstream extent of the interaction located at about 30% of the cavity length (which is closed in this case), so at $x/\delta_{99,0} \approx -5$. For the ventilated cases - diagrams (b) and (c) – it is obvious that the interaction has extended upstream and is initiated right at the front of the cavity ($x/\delta_{99,0} \approx -10$). A clear difference between the two porous plates can be observed: for the smallest hole size, (b), a single leading wave occurs followed by a series of weak secondary waves, whereas for the largest hole size, (c), multiple clear waves are visible at a spacing that corresponds to the hole spacing distance, see Table 2. This reveals that the hole size has a marked impact on the flow field in the upstream region where air exits from the cavity, however, in the downstream region where air enters the cavity there appears no observable difference in the external flow field for the different cases. This will be further analyzed and quantified based on the data from the PIV measurements.
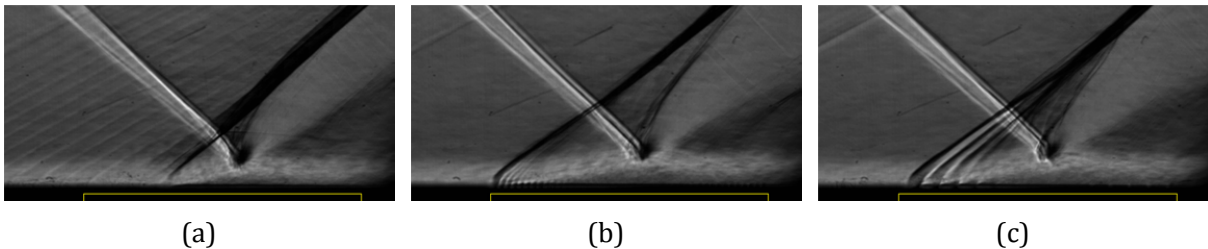

| (a) | (b) | (c) |

Figure 2: Schlieren visualizations; (a) solid (non-porous) plate; (b) porous plate #1; 5% porosity, hole diameter 0.5 mm; (c) porous plate #3; 5% porosity, hole diameter 1.5 mm.

PIV results for the mean structure of the interaction are given in Figure 3, for the same cases as considered in the schlieren visualizations above. Colour contours indicate the horizontal velocity component, while velocity vectors have been down-sampled (1 in 26 for x; 1 in 5 for y) for clarity. The dashed purple line indicates the estimated position of the sonic line, which for the present freestream conditions occurs for $u/U_\infty = 0.638$ (assuming adiabatic flow). The extent of the cavity, ranging from $x/\delta_{99,0} = -9.8$ to 5.8, has been indicated for reference.

For the uncontrolled interaction the dilatation of the low-velocity region is clearly observed, starting at approximately $x/\delta_{99,0} \approx -5$, in agreement with the schlieren visualization (Figure 2a). The maximum thickening of the subsonic region occurs near $x/\delta_{99,0} \approx -1$, so slightly upstream of the extrapolated shock impingement point, while the intersection point between the impinging and reflected shocks is found at a wall-distance of approximately $y/\delta_{99,0} \approx 2.5$. For the ventilated interactions, the interaction is indeed observed to be initiated at the upstream end of the cavity, in agreement with the schlieren data. As a result, the intersection point between impinging and reflected shocks is moved forward and upwards (to $y/\delta_{99,0} \approx 4$). The subsonic flow region dilatation is increased appreciably, however, no or very limited time-averaged reversed flow ($u < 0$) is observed for any of the interactions (see also Section 3.2).
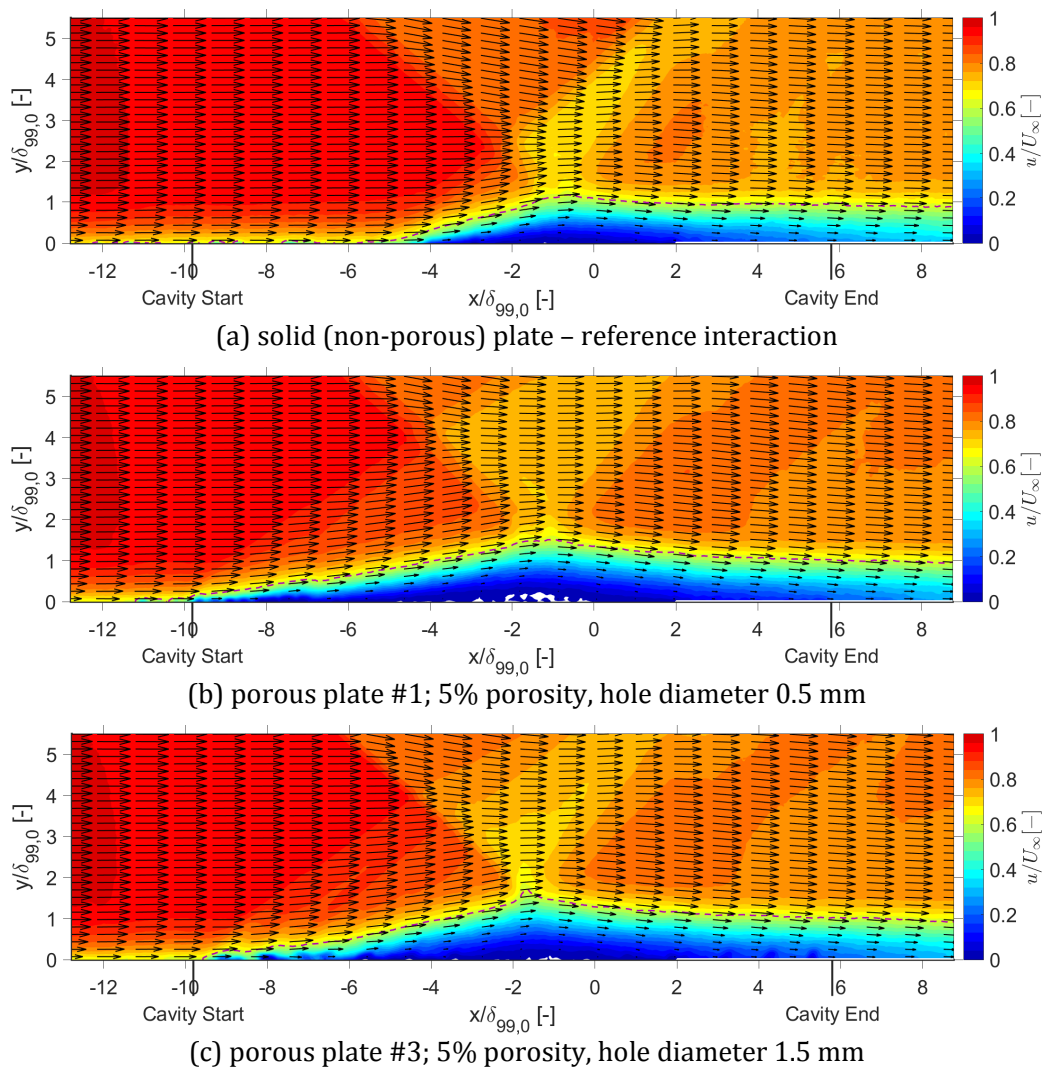

(a) solid (non-porous) plate – reference interaction

(b) porous plate #1; 5% porosity, hole diameter 0.5 mm

(c) porous plate #3; 5% porosity, hole diameter 1.5 mm

Figure 3: PIV velocity fields (streamwise component u) for the SWBLI on different plates; the sonic line is indicated by the dashed purple line.

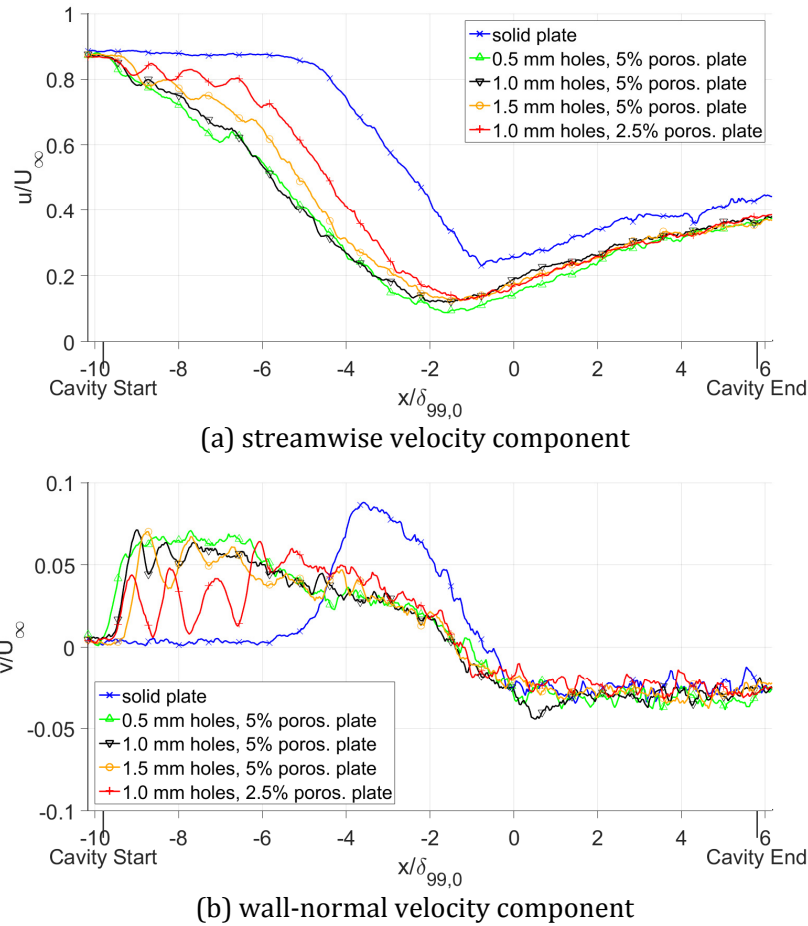(a) streamwise velocity component

(b) wall-normal velocity component

Figure 4: Velocity distributions at $y = 0.5\delta_{99}$.

To further characterize the flow near the wall, and to identify the differences between the porous plates, profiles for the streamwise and wall-normal velocity components have been extracted at a constant wall-normal distance of $y = 0.5\delta_{99}$, see Figure 4. At the beginning of the interaction $u/U_\infty \approx 0.9$ at this height (see Figure 4a), but drops rapidly as soon as the interaction sets in. Minimum values for u/U_∞ are reached at the positions that correspond to the largest thickening of the boundary layer, with $u_{min}/U_\infty \approx 0.23$ for the uncontrolled interaction and $u_{min}/U_\infty \approx 0.09 - 0.12$ for the ventilated cavities, see also Table 3. For the plates of equal porosity (#1,2,3) it can be seen that the minimum velocity reduces as the hole diameter decreases.

Regarding the wall-normal velocity component (Figure 4b), nominally zero values are observed upstream of the interaction, but throughout the interaction first positive, then negative values occur, representing the initial upflow in the interaction and the downflow as the flow again turns back towards to the wall. The location of zero vertical velocity corresponds approximately with that of minimum horizontal velocity. The uncontrolled interaction is more compact, and as such induces a higher maximum upflow ($v_{max}/U_\infty \approx 0.09$). For the ventilated interactions the levels are lower (≈ 0.06 on average for 5% porosity and ≈ 0.03 for 2.5% porosity), but show a strong periodic modulation, dependent on hole size and spacing. For given porosity, the modulation is seen to increase with hole size (hence, with hole separation). A comparable hole effect is not observed for the downstream region where flow enters the cavity, and results are comparable with the non-porous surface. Quantification of these effects, defining representative "upstream" and "downstream" regions, are collected in Table 3. Both mean values and standard deviation for these regions are given, the latter as a measure of the modulation strength.

Table 3. Porous plate interaction properties

plate	porosity ε	hole diameter d_h	$\frac{A_{sep}}{\delta_{99,0}{}^2}$	$\frac{p_{max}}{p_\infty}$	minimum streamwise velocity u/U_∞ at $y = 0.5\delta_{99,0}$	wall-normal velocity v/U_∞ at $y = 0.5\delta_{99,0}$			
						upstream*		downstream*	
						mean	std.dev	mean	std.dev
baseline	0	-	0.44	2.83	0.230	0.003	0.001	-0.025	0.004
#1	5%	0.5 mm	1.09	2.56	0.089	0.065	0.002	-0.031	0.004
#2	5%	1.0 mm	0.89	2.70	0.120	0.058	0.006	-0.030	0.003
#3	5%	1.5 mm	0.71	2.83	0.125	0.055	0.010	-0.029	0.004
#4	2.5%	1.0 mm	0.76	2.81	0.127	0.027	0.013	-0.024	0.004

*The upstream and downstream regions refer to $-9 < x/\delta_{99} < -7$ and $2 < x/\delta_{99} < 5$, respectively.

3.2 Reverse-flow probability

Although no or only marginal flow separation (i.e. flow reversal, $u < 0$) occurs in the mean flow field (see Figure 3), substantial amounts of reverse flow can be observed instantaneously. The local strength of the reversed flow can be expressed by the reverse flow probability $P_{sep}(x, y)$, which is defined as the percentage of occurrences in the individual snapshots that a certain location (x, y) shows reversed flow. The results for the three plates considered previously are given in Figure 5, which reveals that values of 50% or more may locally be reached. In general, the ventilated interactions display more separation, in that larger regions and higher levels of reverse flow probability occur. To provide a quantification of this aspect, an average separated area A_{sep} was calculated, by integrating the separation probability over the domain: $A_{sep} = \int P_{sep}dxdy$ (Giepman et al. 2014). The corresponding values for all plates have been collected in Table 3. These results confirm the increased reverse-flow intensity for the perforated plates in comparison to the baseline interaction, and reveal the significant influence of the hole diameter, with again the strongest influence for the smallest holes (for a given porosity).

(a) solid (non-porous) plate – reference interaction

(b) porous plate #1; 5% porosity, hole diameter 0.5 mm

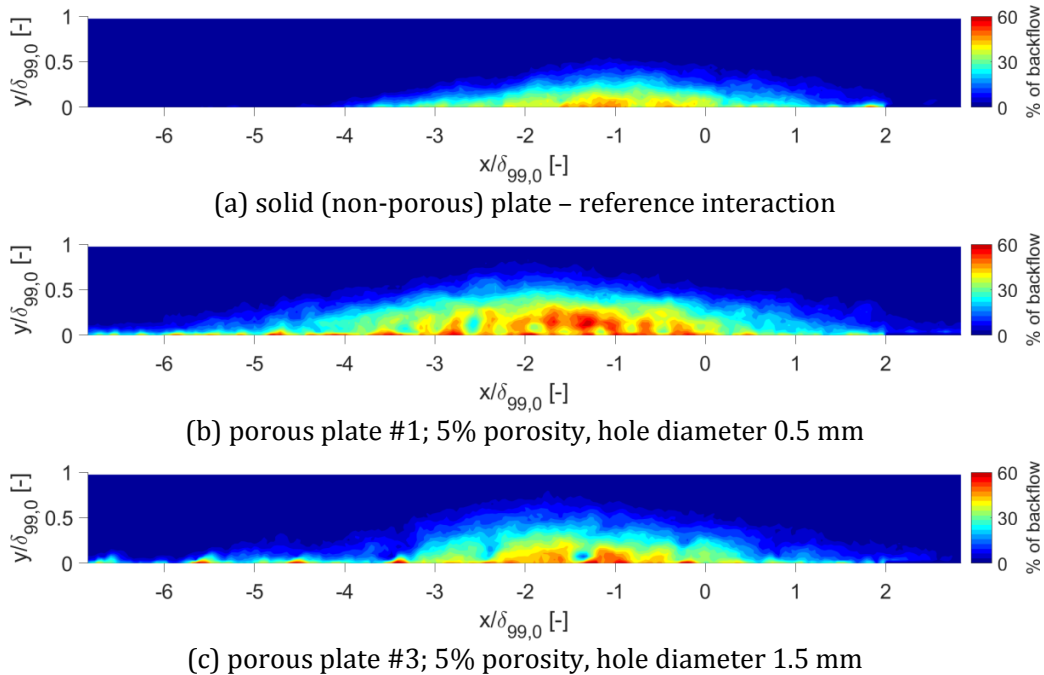(c) porous plate #3; 5% porosity, hole diameter 1.5 mm

Figure 5: Effect of surface porosity on reverse flow probability distribution P_{sep}

3.3 Pressure fields

Pressure fields were derived from the velocity data by the procedure described in section 2.4 and results are shown in Figure 6 for the three selected plates considered in the previous cases. Flow vectors are again included, to assist the interpretation of the pressure fields in connection to the flow velocity. The general pressure topology is very comparable for all three interactions: from the upstream flow region, clear pressure increases are observed over the impinging and separation shocks, whereas a further compression occurs after their intersection, in the region following the transmitted and reflected shocks. This is subsequently followed by a pressure decrease, due to the expansion fan originating from the crest of the interaction, as the flow is directed again towards the wall. Further downstream the recompression of the flow can be seen.

Comparing the different interactions, it is obvious that for the porous plates the compression associated to the interaction starts much more upstream, at the front of the cavity. The high-pressure region behind the shock-intersection point is accordingly expanded, however, the intensity of the pressure increase is reduced (the maximum observed pressure level is included in Table 3). Also the pressure increase near the wall occurs more gradually, as is the pressure recovery towards the end of the cavity.

(a) solid (non-porous) plate – reference interaction

(b) porous plate #1; 5% porosity, hole diameter 0.5 mm

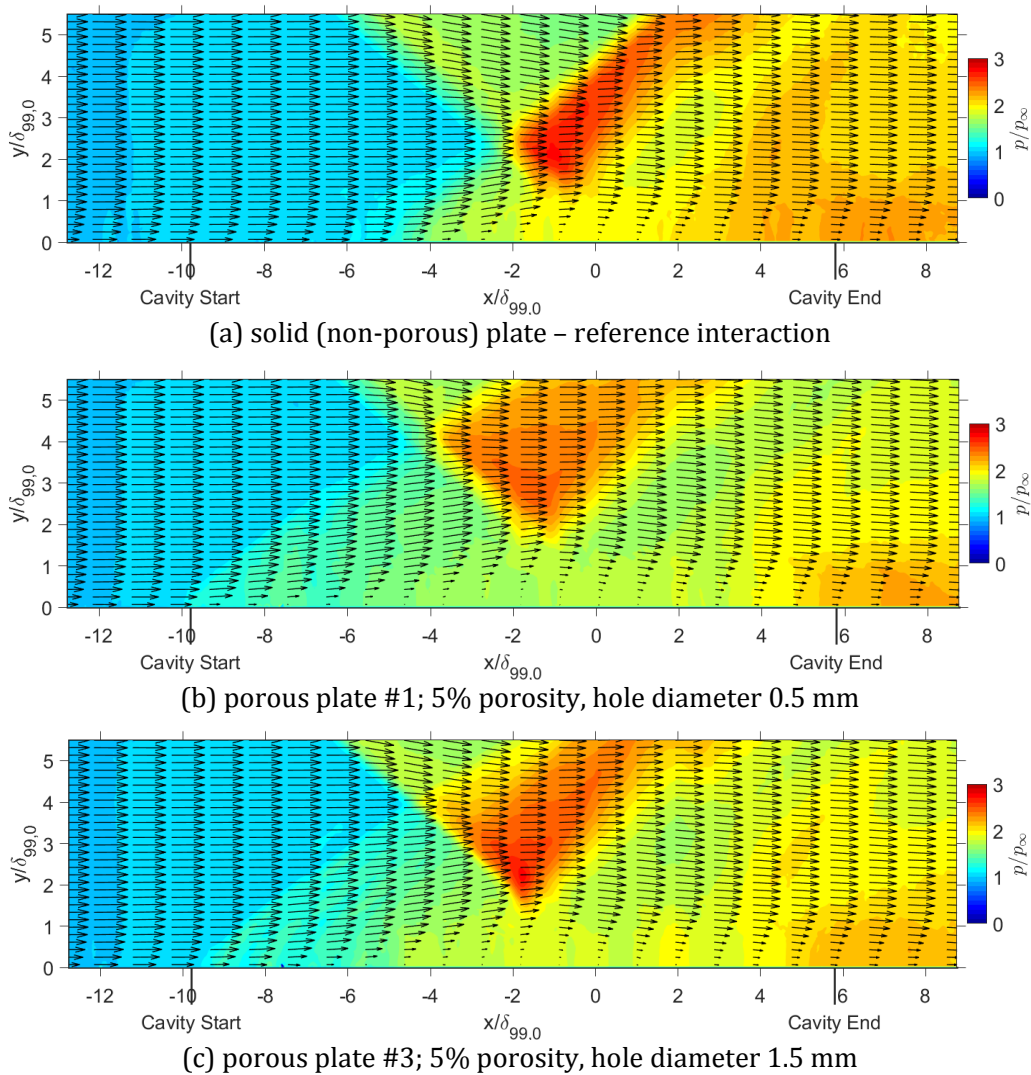(c) porous plate #3; 5% porosity, hole diameter 1.5 mm

Figure 6: Integrated mean pressure fields for the SWBLI on different plates.
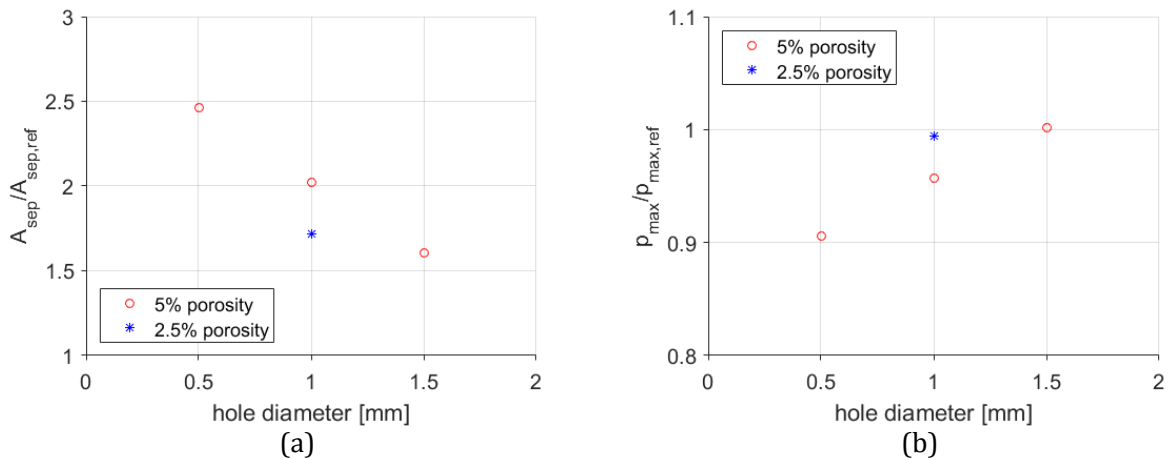
Figure 7: Porous plate interaction properties; (a) integrated reverse-flow probability; (b) maximum field pressure; values are scaled with those of the uncontrolled interaction.

4   Conclusions

Planar Particle Image Velocimetry (PIV) has been used to characterize the interaction between an impinging oblique shock wave and a turbulent boundary layer over a ventilated cavity covered by a porous surface, at a Mach number of 1.86 and a Reynolds number based on the incompressible momentum thickness of 19,000. The interaction was induced by a 8.8° wedge, with the extrapolated impinging shock intersecting at 63% of the cavity length. Pressure has been estimated from the velocity data by integration of the pressure gradient inferred from the momentum equation, under the approximation of steady, adiabatic, two-dimensional flow.

It is confirmed that the application of surface porosity results in an appreciable extension of the interaction in the longitudinal direction. In all cases investigated, the outflow in the upstream part of the cavity appears to be of sufficient strength to trigger the interaction to start directly at the beginning of the cavity. There is a clear influence of the hole size (and porosity) on the flow field character. Different parameters to characterize this effect have been collected in Table 3 that allows to compare the performance of the difference plates in more detail. In addition, two of these parameters have been plotted in Figure 7 as a function of hole diameter, which are the integrated reverse-flow probability A_{sep} and the maximum field pressure p_{max}; all values have been scaled with those of the uncontrolled interaction on the solid plate. The results show that, as expected, the impact on the interaction increases with the degree of porosity of the plate. However, for given porosity there is a marked influence of the hole diameter, with the smallest hole diameter giving the strongest effect: A_{sep} is increased by about 150%, while p_{max} is reduced by 10%.

References

Babinsky H, and Harvey J (2011) *Shock Wave-Boundary-Layer Interactions*. Cambridge University Press

Bruce PJK, and Colliss SP (2015) Review of research into shock control bumps. *Shock Waves* 25: 451-471

Bur R, Corbel B, and Délery J (1998) Study of passive control in a transonic shock wave / boundary-layer interaction. *AIAA Journal* 36:394-400

Délery JM (1985) Shock wave/turbulent boundary layer interaction and its control. *Progress in Aerospace Sciences* 22:209-280

Délery JM, and Bur RS (2000) The physics of shock wave/boundary layer interaction control: last lessons learned. *ECCOMAS 2000*, Barcelona, Spain, 11-14 September 2000

Doerffer P, and Bohning R (2000) Modelling of perforated plate aerodynamics performance. *Aerospace Science Technology* 4:525-534

Dolling DS (2001) Fifty Years of Shock-Wave/Boundary-Layer Interaction Research: What Next? *AIAA Journal* 39:1517-1431

Gefroh D, Loth E, Dutton C, and McIlwain S (2002) Control of an oblique shock/boundary-layer interaction with aeroelastic mesoflaps. *AIAA Journal* 40:2456-2466

Giepman RHM, Schrijer FFJ, and van Oudheusden BW (2014) Flow control of an oblique shock wave reflection with micro-ramp vortex generators: effects of location and size. *Physics of Fluids* 26:066101

Gramola M, Bruce PJK, and Santer M (2018) Experimental FSI study of adaptive shock control bumps. *Journal of Fluids and Structures* 81:361–377

McCormick DC (1993) Shock/boundary-layer interaction control with vortex generators and passive cavity. *AIAA Journal* 31:91-96

Panaras AG, and Lu FK (2015) Micro-vortex generators for shock wave/boundary layer interactions. *Progress in Aerospace Sciences* 74:16-47

Ragunathan S (1988) Passive control of shock-boundary layer interaction. *Progress in Aerospace Sciences* 25:271-296

Souverein L, and Debiève J-F (2010) Effect of air jet vortex generators on a shock wave boundary layer interaction. *Experiments in Fluids* 49:1053-1064

Stanewsky E, Délery JM, Fulker M and Geissler W (1997) EUROSHOCK – Drag reduction by passive shock control. *Notes on numerical fluid mechanics*, vol. 56, Vieweg Verlag

Titchener N, and Babinsky H (2015) A review of the use of vortex generators for mitigating shock-induced separation. *Shock Waves* 25:473-494

van Gent PL, van Oudheusden BW, and Schrijer FFJ (2018) Determination of mean pressure from PIV in compressible flows using the Reynolds-averaging approach. *Experiments in Fluids* 59:41.

van Oudheusden BW (2008) Principles and application of velocimetry-based planar pressure imaging in compressible flows with shocks, *Experiments in Fluids* 45:657-674

van Oudheusden BW (2013) PIV-based pressure measurement. *Measurement Science & Technology*, 24:032001

Webb N, Clifford C, and Samimy M (2013) Control of oblique shock wave/boundary layer interactions using plasma actuators. *Experiments in Fluids*, 54:1545